Rapid multi-plane phase-contrast microscopy reveals torsional dynamics in flagellar motion

SOHEIL MOJIRI,[1] SEBASTIAN ISBANER,[1] STEFFEN MÜHLE,[1] HONGJE JANG,[1] ALBERT JOHANN BAE,[2] INGO GREGOR,[1] AZAM GHOLAMI,[2,3] AND JÖRG ENDERLEIN[1,*]

[1] *III. Institute of Physics – Biophysics, Georg-August-University, 37077 Göttingen, Germany*
[2] *Max-Planck-Institute for Dynamics and Self-Organization, 37077 Göttingen, Germany*
[3] *Cluster of Excellence "Multiscale Bioimaging: from Molecular Machines to Networks of Excitable Cells" (MBExC), Georg-August-University, 37077 Göttingen, Germany*
[*] *jenderl@gwdg.de*
http:www.joerg-enderlein.de

Abstract: High speed volumetric optical microscopy is an important tool for observing rapid processes in living cells or for real-time tracking of sub-cellular components. However, the 3D imaging capability often comes at the price of a high technical complexity of the imaging system and/or the requirement of demanding image analysis. Here, we propose a combination of conventional phase-contrast imaging with a customized multi-plane beam-splitter for enabling simultaneous acquisition of images in eight different focal planes. Our method is technically straightforward and does not require complex post-processing image analysis. We apply our multi-plane phase-contrast microscope to the real-time observation of the fast motion of reactivated *Chlamydomonas* axonemes with sub-µm spatial and 4 ms temporal resolution. Our system allows us to observe not only bending but also the three-dimensional torsional dynamics of these micro-swimmers.

1. Introduction

Optical microscopy has seen a tremendous development over the past decades, in particular with the evolution of super-resolution microscopy. However, even in the realm of diffraction-limited microscopy, there is still plenty of room for further developments and new approaches. The ideal microscope should combine high spatial resolution with high temporal resolution, together with the ability of three-dimensional imaging, and ideally without the requirement of labeling. Here, we present such an instrument which allows for high speed, three-dimensional imaging with diffraction-limited resolution on unlabeled biological specimens.

Recently, new multi-plane imaging microscopes were introduced that circumvent the above mentioned drawbacks [1]. They use mainly two fundamentally different approaches. The first is based on dedicated and chromatically-corrected diffraction gratings for generating many images, each of them relating to a different focal plane [2–5]. The other uses beam-splitters and mirrors for generating multiple images together with multiple lenses with different focal lengths to provide different optical path lengths [6–8] or by remote focusing [9]. Alternatively, instead of multiple lenses, one can create different optical path lengths by introducing tilts in orientation of mirrors associated with cascaded beam-splitters which provide a powerful approach that can generate, in principle, an arbitrary number of focal planes [10]. One important advantage of this cascaded design is that it can be realized with a single piece of glass [11,12] making the optics extremely robust against mechanical drift and thus avoiding the need for frequent readjustments.

Here, we combine the single-component compound prism as introduced in Ref. [12] with a phase-contrast microscope to enable rapid, label-free, 3D yet robust and easy-to-use microscopy.

As an exemplary application of this system, we use it to observe the exceptionally fast motion of single flagella (axonemes) of the alga *Chlamydomonas*.

Flagella and cilia are upon the most astounding biological entities. These motile cellular appendages are essential for many functions from single cells to higher organisms. Accordingly, the mechanisms behind the dynamics of flagella and cilia have been subject of many studies. The structure of their cytoskeletal core, the axoneme, is highly conserved for all basically all species. It consists of nine microtubule doublets (MTDs) forming a cylinder around a tenth doublet on its axis. The diameter of the cylinder is about 200 nm, whereas its length can reach more than 150 μm. Dynein motor proteins are cross-linking the nine neighbouring MTDs in the outer ring. The radial and longitudinal polarities of the MTDs make the axoneme an inherently chiral structure [13]. Upon hydrolyzation of adenosine triphosphate (ATP) the dynein motors walk along the MTDs pulling their respective right neighbour towards the basal end [13–15]. This drives a regular three-dimensional motion of the axoneme [16,17]. Such a motion occurs in a rapid fashion. For instance, isolated and reactivated axoneme of the model organism *Chlamydomonas* algae can beat with a frequency of >100 Hz [18].

When kept in a closed observation chamber, active flagella will accumulate at either the top or bottom surface of the chamber. This already indicates that their motion is intrinsically three-dimensional. However, nearly all experimental studies of the dynamics of axonemes are two dimensional. This is partially due to the fact that the study of short and fast beating axonemes requires rapid imaging in three dimensions that is still technically challenging. As will be demonstrated below, with our new 3D imaging system we are able to follow the full three-dimensional beating of single flagella, measuring not only their bending but also torsion dynamics with high temporal resolution.

2. Methods

2.1. Multi-plane phase-contrast microscope

A schematic of our custom-built multi-plane phase-contrast microscope is shown in Fig. 1. The system allows for parallel recording of eight wide-field images in eight focal planes that are evenly spaced along the optical axis. The system is based on the commercial microscope IX71 from Olympus (Olympus Deutschland GmbH, Hamburg, Germany). The collimated light of a white-light source (U-LH100L-3 halogen lamp, Olympus) is sent through a condenser annulus (IX-PH3, Olympus) and focused by a condenser lens (IX2-LWUCD, Olympus) onto the sample for realizing Köhler illumination. Scattered and transmitted light are collected by a Zernike phase-contrast objective (UPLFLN 60XOIPH, 60× 1.25 NA, Olympus), which shifts the phase of the transmitted light by $-\pi/2$ with respect to the scattered light resulting in destructive interference between scattered and non-scattered light.

This generates a phase-contrast image when focused by the tube lens onto a camera. Before imaging, a commercial 2 x 4 beam-splitter prism (patent EP3049859A1, Scoptonic imaging technologies, Torun, Poland) splits the collected light into eight beams with different optical path lengths corresponding to eight different focal planes in the sample (see section 6.2 in the supplementary information of Ref. [12] for a detailed explanation of the prism design). These focal planes are equally spaced with a distance of ~359 nm along the optical axis, thus spanning a total volume of ~2.5 μm depth. Four of the light beams exit the beam-splitter prism in a direction parallel to the incoming light, and four exit the prism in a perpendicular direction. Each set of these four beams is imaged onto a separate camera so that the images of the different focal planes are positioned next to each other on the camera chip (see Fig. S1a,b in Supplement 1). The rectangular field stop aperture in the focal plane of the tube lens with the opening size ~2.45×2.45 mm² adjusts the field of view and prevents overlap between adjacent images on the cameras. Since the prism's geometry and refractive index is fixed, the inter-plane distance can be changed only by changing the magnification of the imaging system. Image acquisition
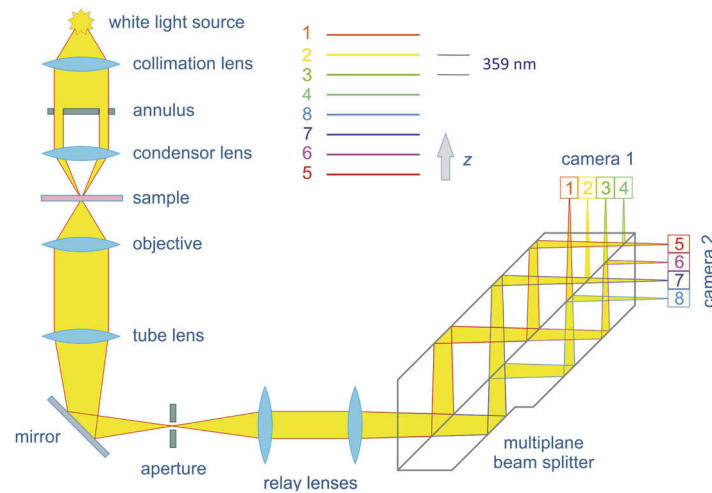
Fig. 1. Schematic of the multi-plane phase-contrast microscope. Light from a white-light source is sent through an annular aperture and focused onto the sample for high-angle illumination. Transmitted and scattered lights are collected with a Zernike phase-contrast objective (oil immersion, 60× magnification, 1.25 NA), focused by the tube lens through a slit aperture, and then sent through two relay lenses (that increase magnification to 80×) towards a custom-made multi-plane beam splitter. This splitter generates eight laterally shifted image replicas with an increasingly longer optical path length, corresponding to eight different focal planes in the sample. These eight images correspond to eight focal planes in the sample separated by 359 nm (in aqueous solution), and two sCMOS cameras record them. The slit aperture limits the field-of-view and prevents overlap between neighboring images on the cameras.

by the two cameras is synchronized with an external trigger. Data acquisition is controlled by the open-source microscopy software µManager [19]. Table S1 in Supplement 1 lists the specifications of all optical components employed in the setup.

2.2. Setup calibration

The beam-splitter was designed to render two times four adjacent channels with a lateral distance of $d = 3.2$ mm in between, which fits in size to the width of the 13.3 mm×13.3 mm pixel area of a sCMOS detector (ORCA-Flash 4.0 V2, Hamamatsu). The second camera is shifted out of focus by a distance of $4d/n$, where $n = 1.46$ is the refractive index of the prism material. This allows one to obtain an optical path difference of $\sim d/n$ between sequential planes. To calibrate this system, we performed a z-scan of immobilized light-scattering latex microspheres of 500 nm diameter. These microspheres were spin-coated on a glass coverslide, and imaged using an oil immersion phase objective (UPLFLN 60XOIPH, 1.25 NA, Olympus) and the relay lens system as shown in Fig. 1. This relay lens system increases the total magnification to 80×. Z-scanning was realized by moving the objective over an axial range of 7 µm with 100 nm step size. Figure 2(a) displays an example of a multi-plane phase-contrast image of microspheres at one z-scan position.

Lateral (305 nm) and axial (1.25 µm) resolution of the optical system (at the laser excitation wavelength $\lambda = 520$ nm) was determined by measuring the full-width-at-half-maximum (FWHM) of single microsphere images. A plot of the total intensity recorded in each of the eight planes as a function of the axial position of the objective, together with Gaussian fits, is shown in Fig. 2(b). A linear fit of their maximum position as a function of the objective's axial position, Fig. 2(c), yields an average inter-plane distance of 430 nm. The corresponding inter-plane distance in water
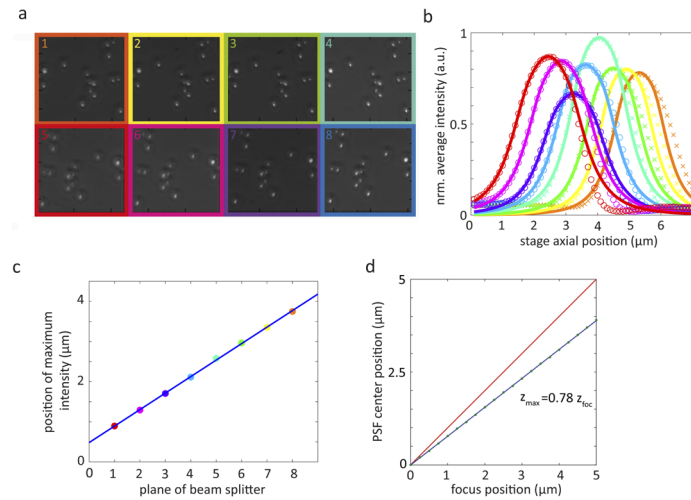
Fig. 2. Inter-plane distance and brightness calibration. (a) Example of the eight images of scattering microspheres recorded by the multi-plane wide-field microscope. In this example, microspheres are in focus in nominal plane #4 (b) Normalized average intensity in each image plane as a function of axial scan position (for axial scan steps of 100 nm). Crosses (for camera 1) and open circles (for camera 2) represent measured data, solid lines are Gaussian fits. (c) Linear fit of positions of intensity maxima from panel (b). The fit yields an average inter-plane distance of 430 nm (for oil immersion). (d) Relative shift of focal plane position in water (blue line) with respect to oil (red line). Open circles are the result of a wave-optical calculation of imaging in water, the blue solid line is a linear fit to this result. It shows that close to the glass interface, we still find a linear relationship between focal plane position and the objective's axial position, but inter-plane distance in water is by a factor of 0.78 smaller than in oil.

shrinks by a factor of 0.78 due to the refractive index mismatch between immersion oil and water, as numerically calculated using the wave-optical theory developed by Wolf and Richards [20,21]. The result of these calculations, Fig. 2(d), shows how the axial center of the point spread function (PSF) in water (blue line) deviates from its position that it would have in glass/oil (red line). Thus, our multi-plane system allows us to record a sample volume of $\sim40\times40\times2.5$ μm^3 in an aqueous medium.

The area under each curve in Fig. 2(b) is the relative amount of light that is recorded in each of the eight channels. These numbers, ε (plane #), are required later for correcting the slight brightness variations between different planes that originate from a non-perfect division of light by the beam splitter ($\pm11.7\%$ s.d. of averaged brightness).

2.3. Work flow from acquired raw data to a registered 3D image stack

Image acquisition. Images in eight focal planes, divided into two groups of four upper and four lower planes, are simultaneously acquired by camera 1 and camera 2, respectively (Fig. S1a,b in Supplement 1). Images of camera 1 are horizontally flipped to have the same orientation as those of camera 2.

Brightness correction, image conversion, and Gaussian filtering. Intensity values in all eight image planes are balanced by multiplying them with the corresponding weight factors $1/\varepsilon$ (Fig. S1c in Supplement 1). All image values are inverted to negative numbers for contrast enhancement and better visualization of axonemes (Fig. S1c in Supplement 1). For noise reduction, a 2D Gaussian kernel (imgaussfilt function in MATLAB) with a standard deviation

of σ = 2 pixels (~162 nm) is used for low-pass frequency filtering (Fig. S1d in Supplement 1). The optimal σ value is selected to match the width of the PSF (standard deviation of PSF intensity distribution) of our microscope (~172 nm) - increasing σ further lead to a reduced accuracy in determining the three-dimensional contour of the axonemes. To check whether more sophisticated image filtering procedures show better performance, we applied also a more sophisticated noise filtering method based on a windowed Fourier transform [22,23]. This filter is available for MATLAB [24] and was applied without modifications. As it occurred, it did not lead to more accurate results for the final axoneme contour tracking (see Fig. S7 in Supplement 1), and we therefore kept 2D Gaussian filtering, which was also by 2-3 orders of magnitude faster than the windowed Fourier transform routine.

Subtraction of median intensity. The median intensity of images determined over all frames (Fig. S1e in Supplement 1) is subtracted from each image plane to remove all contributions from immobile and static sources. This also increases the SNR by a factor of 3 to 5 times, depending on signal strength (Fig. S1f in Supplement 1).

Co-registration of planes. The eight raw images have a small shear relative to each other (Fig. S2a in Supplement 1), which needs to be registered. This is done by calculating the two-dimensional cross-correlation of each plane with respect to one reference plane (either plane #4 or plane #5 close to the center of the stack) (Fig. S2b in Supplement 1). The peak position of this cross-correlation gives the direction and value of the relative shift of the considered plane with respect to the reference plane. This shift estimation is refined by repeating the procedure on Fourier up-sampled images [25]. Using these values, all images are registered to a common frame with sub-pixel precision (Fig. S2c,d in Supplement 1). Non-overlapping image borders arising from registration are cropped in the final aligned image stack (Fig. S2d,e in Supplement 1).

Image sharpening. The diameter of *Chlamydomonas* axonemes (~150 nm) is smaller than the resolution limit of the microscope. To enhance the localization of axonemes in all spatial dimensions, we perform a simple 3D deconvolution. The basal end of the axoneme is slightly (~10%) thicker than its distal end [18], but otherwise, all axonemes show an almost homogeneous image intensity along their contour length. Thus, an axoneme's shape can be effectively considered as a continuous one-dimensional line in three-dimensional space. This *a priori* information can be used for three-dimensional image deconvolution. Each frame of the multi-plane image stack is deconvolved using a pre-calculated aberration-free PSF at the interface of the glass coverslide and water (Fig. S3a in Supplement 1). This PSF is calculated using the wave-optical theory of Richards and Wolf [20,21] and the optical parameters of our setup (imaging wavelength λ_{peak} of 585 nm, numerical aperture N.A. of 1.25, image magnification of 80×, principal focal length of 3 mm for the objective, and water and oil refractive index values of n_{water} = 1.33 and n_{glass} = 1.52, respectively). Within a small axial distance from the surface, this PSF remains an excellent approximation of the actual one despite refractive index mismatch, as can be seen by comparing its shape at a nominal focus position of ~1.5 μm above the surface (Fig. S3b in Supplement 1) with the aberration-free PSF directly at the surface (Fig. S3a in Supplement 1). For deconvolution, we performed ten iterations using a 3D Lucy-Richardson algorithm (deconvlucy function in MATLAB), which results in a sharpening of the axoneme contour by a factor of ~2 in all directions. Figures S3c,e in Supplement 1 present an axoneme image maximum-projected along the optical axis and along the y-direction, respectively. Corresponding deconvolved images are shown in Fig. S3d,f in Supplement 1.

2.4.   Axoneme isolation and reactivation

Axonemes are isolated from wild-type *Chlamydomonas reinhardtii* cells, strain SAG 11-32b. They were grown axenically in TAP (tris-acetate-phosphate) medium on a 12 h/12 h day-night cycle. Flagella were isolated using dibucaine [26,27], then purified on a 25% sucrose cushion,

and demembranated in HMDEK (5 mM MgSO$_4$, 30 mM HEPES-KOH, 1 mM EGTA, 50 mM potassium acetate, 1 mM DTT, pH 7.4) supplemented 0.2 mM Pefabloc. The membrane-free axonemes were re-suspended in HMDEK plus 1% (w/v) polyethylene glycol (m$_w$ = 20 kg/mol), 30% sucrose, 0.2 mM Pefabloc and stored at -80°C. To perform reactivation experiments, axonemes were thawed at room temperature, afterward kept on ice, and used for up to 1 hr. Thawed axonemes were diluted in HMDEKP reactivation buffer containing 1 mM ATP and infused into 100 μm deep flow chambers, built from cleaned glass and double-sided tape. The height of the chamber is 10 times larger than the typical length of the axonemes (10 μm). Therefore, we expect to have a negligible effect of confinement on the swimming dynamics. The glass surface was blocked using casein solution (from bovine milk, 2 mg/mL) to avoid attachment of axonemes to the substrate.

2.5. Axoneme contour 3D tracking

Tracking of an axoneme starts with finding its 2D contour in the 2D maximum intensity projections along the optical axis using a gradient vector flow (GVF) snake algorithm [28,29] (Fig. S4a,b in Supplement 1). For the first frame, the user selects a region of interest that should contain only one single axoneme. Then, the user initializes contour determination by drawing a polygonal line along the contour of the axoneme (Fig. S4c in Supplement 1). This polygonal line is interpolated to N = 30 points and is used to estimate the contour length and as a starting guess for the snake algorithm (Fig. S4d in Supplement 1). This initial guess is used to calculate the GVF with 20 iterations and a GVF regularization coefficient of $0 < \mu < 1$, to deform the snake accordingly to the contour in the next frame. The GVF regularization coefficient is set depending on the noise level of images. We set a fixed value of $\mu = 0.1$ in GVF algorithm for all of our axoneme data because we have a similar level of noise over time. We have adapted the original GVF algorithm by Xu and Prince for open boundary conditions [29].

In the next step, a height profile $h_k(z)$ is created for each segment k, averaging the intensity over pixels of the segment (Fig. S4e in Supplement 1). This profile is fitted with a 1D Gaussian (Fig. S4f in Supplement 1). The z-position of the maximum of this fit yields the axial coordinate z_k of the segment, and together with its lateral positions x_k and y_k constitutes the 3D coordinates of segment k. An installation file "AxonemeTracking3D.mlappinstall" for a platform-independent MATLAB app together with its source code ("source code.zip") and sample data ("testdata.mat") can be downloaded at the Göttingen Campus repository [30]. This app executes the contour determination and contour discretization of 3D axoneme images. The repository provides also the commented MATLAB program 'FlagellumAnalysisExample.m' together with tracking data ('result_tracking22.mat') of the axoneme analyzed in Fig. 4(a),(b) which demonstrates the calculation of curvature and torsion from a discretized contour, and their graphical display.

The tracking routine yields a discrete approximation of an axoneme's contour represented by a set of 30 three-dimensional positions $\mathbf{r}_i = (x_i, y_i, z_i)$, $i = 1 \ldots 30$. For each time frame, these points constitute a polygonal chain, which is least-square fitted with polynomial functions of the form $\sum_{m=0}^{M} c_m i^m$, where the c_m are fit coefficients. We have set $M = 6$ (6th order polynomial) for fitting the lateral x,y-positions, and $M = 3$ (3rd order polynomial) for the axial z-positions.

To suppress nonphysically large curvature values at the contour ends, we regularized the contour by extending it on both ends with short mirror-symmetric patches before polynomial fitting. More precisely, at the $i = 1$ end, we add additional points via $\mathbf{r}_{1-j} = 2\mathbf{r}_1 - \mathbf{r}_{1+j}$, and at the $i = 30$ end, via $\mathbf{r}_{30+j} = 2\mathbf{r}_{30} - \mathbf{r}30 - j$. This changes the absolute curvature values at the ends of an axoneme, but impacts only slightly the results in the middle (see Fig. S6 in Supplement 1). For our final analysis, we have chosen a padding with three additional points on each end.

3.   Results

Using the multi-plane phase-contrast microscope, we recorded movies of beating axonemes with 272 volumetric images per second. An example of four of such consecutively taken volumetric images are shown in Fig. 3(a), where the color encodes the third dimension. In each of the volumetric images, the three-dimensional contour of an axoneme was discretized, and the resulting discrete lateral (x_j and y_j) and axial (z_j) positions were fitted with polynomial functions. The result is a four-dimensional representation $\mathbf{r}(s,t)$ of an axoneme's contour as a function of time t and arc length s, where we have $|\partial \mathbf{r}(s,t)/\partial s| \equiv |\mathbf{r}'(s,t)| = 1$. Discretized contours and fit results for the four images in Fig. 3(a) are shown in Fig. 3(b). As can be seen from the projections into the different coordinate planes, the discretized axial positions show ~10-fold bigger jitters than the lateral positions. We estimated the accuracy of the polynomial contour fit from the standard deviations between fitted and discretized position values, and find a lateral position accuracy better than 20 nm, and an axial position accuracy better than 120 nm (see Fig. S7 in Supplement 1).
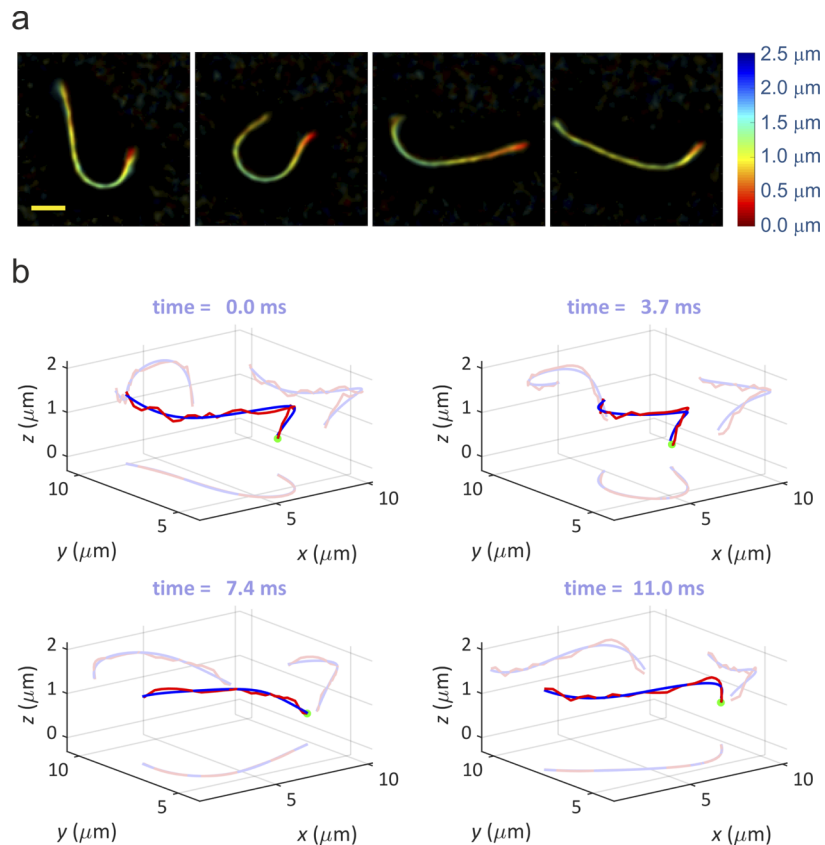

Fig. 3. Three-dimensional recording of axoneme motion. (a) Four consecutive raw images recorded with the multi-plane phase-contrast microscope. Color encodes the axial position (see color bar), the yellow bar in the leftmost panel has a length of 2 μm. (b) Discretized axoneme contours (red) and fitted polynomial curves (blue) for the four images shown in (a). For a better visibility, the respective projections into the three coordinate planes are also shown. The green dot indicates the basal end of the axoneme.

From the polynomial representation of the axonemal contours, spatio-temporal profiles of curvature $\kappa(s,t)$ and torsion $\tau(s,t)$ are calculated by [31]

$$\kappa(s,t) = |\mathbf{r}''(s,t)| \tag{1}$$

$$\tau(s,t) = \frac{[\mathbf{r}'(s,t) \times \mathbf{r}''(s,t)] \cdot \mathbf{r}'''(s,t)}{\kappa^2(s,t)} \tag{2}$$

where a prime denotes differentiation with respect to arc length s. It should be emphasized that torsion quantifies the out-of-plane bending of an axoneme and can only be extracted from its full three-dimensional contour.

We measured the contour dynamics of 35 axonemes in a normal aqueous-like swimming medium. All observed axonemes move close and parallel to the coverslide surface of the observation chamber due to hydrodynamic interactions with the surface [32,33]. All except one (with beat frequency of ~12 Hz) of them showed a counter-clockwise (CCW) circular motion when viewed from above. The CW rotation has been observed in previous studies in 40% of axonemes isolated from mutants lacking outer dynein arm ODA1 [18] 70% of axonemes
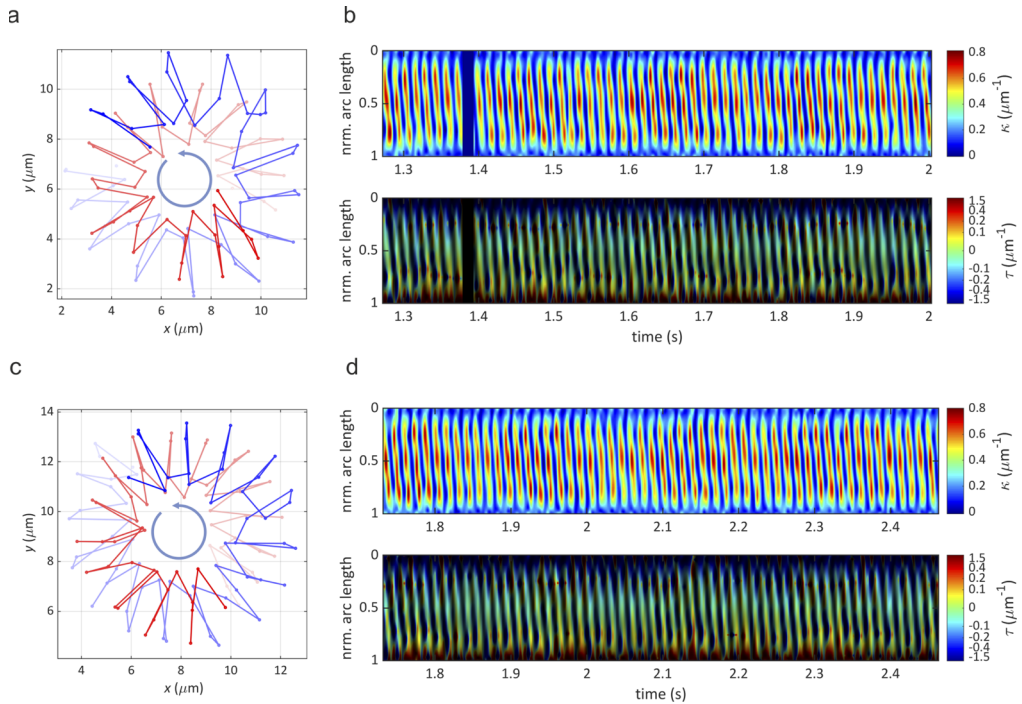

Fig. 4. Analysis of flagellar motion. (a,c) Circular motion of basal end (red) and distal (blue) tip of two CCW-moving flagella as seen from above the surface. From light to dark, the shading indicates progression in time. The time between two discrete points of trajectory is 3.7 ms. (b,d) Space-time plots of curvature and torsion for the same flagella, as shown in (a,c), over an observation time of ~0.7 s. The dark vertical lane at ~1.4 s corresponds to a short excursion of the distal tip of the axoneme beyond the axial range of our observation volume and is excluded from the analysis. Vertical axis is the *normalized* arc length ($s = 0$ at basal end, $s = 1$ at distal tip). In the torsion plots, color encodes torsion values, while brightness is proportional to curvature. This suppresses nonphysical torsion values in regions of low or zero curvature, where torsion is ill-defined. Note also the strongly non-linear color mapping (see color bar), which makes the small torsion values better visible.

isolated from inner dynein arm IDA7 mutants [18] or in 18% of axonemes reactivated at low ATP concentrations between 50 μM and 400 μM [18,34]. For further analysis, we present here two CCW moving flagella with nearly identical swimming radius and beat frequency (~73 Hz, determined from Fourier power spectra of space-time curvature plots (see also Fig. S8 in Supplement 1). Projections (*x*,*y*-coordinates) of the swimming contours of the basal end and distal tip for both flagella are shown in Figs. 4(a) and 4(c). The basal end traces a smaller circle and swims closer to the surface than the distal end (see Fig. S5 in Supplement 1 for axial localization of basal, distal and midpoint along the axonemal contour). Axonemal contour clearly follows a helical path (see Fig. 3(b) and supplemental movies Visualization 1 and Visualization 2).

Space-time plots of curvature and torsion for both flagella are presented in Figs. 4(b) and 4(d) (see supplemental movies Visualization 1 and Visualization 2 for the corresponding three-dimensional flagellar motion). The plots show curvature waves that start at the basal end ($s = 0$) and move towards the distal tip. This is accompanied by torsion waves that start with negative torsion values at the basal end and gradually change sign until they finish with positive torsion values at the distal tip. These torsion wave dynamics are nearly identical for both the presented axonemes.

The observed bending and torsion dynamics demonstrate the fundamentally *three-dimensional* nature of flagellar motion. We propose that the observed torsional waves are closely connected to the intrinsic chiral structure of the axoneme and to twist induced by dyneins. According to the model developed in Refs. [35] and [36], dynein motors induce sliding between neighboring MTDs, which does not only drive axoneme bending but also induces twisting of the axoneme. Dyneins transiently attach with their MT binding domains to neighboring MTDs and walk towards the basal end, which causes distal-end directed sliding forces between neighboring MTDs [37]. In an untwisted axoneme, such a motion will induce a positive twist (as seen at the basal end), which should be observable as a positive torsion in a bent axoneme. Because we observe a periodically negative torsion in each beat cycle close to the basal end, we suggest the existence of an intrinsic negative twist at the beginning of each beat cycle. This is visualized in Fig. 5(a) as a side view of sinistrally twisted MTDs close to the basal plate of an axoneme
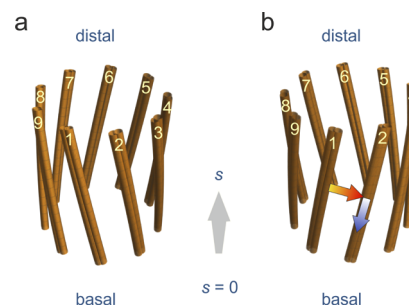

Fig. 5. Twist of an axonemal structure. Shown are the nine MTDs around the circumference of an axoneme. (a) Intrinsic sinistral twist close to the basal end. (b) Dynein-induced dextral twist close to the distal tip. The red arrow indicates the direction along which dynein motors reach from their MTD of attachment to the neighboring MTD on which they bind. The blue arrows indicate the walking direction of the dynein motors. The action of the dyneins leads to sliding of MTDs with respect to each other. Due to structural connections between MTDs (e.g., by nexin proteins), this is likely to induce a local twist of the axoneme structure, as shown in 4(b). If the whole structure is additionally bent, this twist will translate into torsion (with same chirality as the twist), as experimentally observed at the basal end and distal tip of the bare axonemes.

to which the axonemal MTDs are fixed (numbering of MTDs in this figure follows Ref. [38]). Then, the dynein's activity unwinds this negative intrinsic twist, reducing negative torsion at the basal end and generating positive twist and torsion at the initially twist- and torsion-free distal end (Fig. 5(b)). Such a change in torsion sign has also been observed in quail sperm flagella [39]. Bending of the axoneme then translates this twist into observable torsion with the same sign.

4.   Discussion and conclusion

We have developed a multi-plane phase-contrast microscope that allows for volumetric imaging close to diffraction-limited resolution and with frame rates of several hundred volumes per second. For applications that require imaging over a deeper volume than that observed in the current paper, the axial dynamic range can be tuned by changing image magnification. For imaging *Chlamydomonas* axonemes, we have chosen an image magnification that provides an axial dynamic range of ~2.5 μm image depth. This enabled us to follow the full beating dynamics of the short *Chlamydomonas* flagella with exceptional high 3D spatial resolution, allowing us to observe not only the bending but also torsion dynamics of axonemal motion. We observed torsional waves that started with a negative sign at the basal end, and then gradually changed their sign while travelling along the axonemal contour towards the distal end. We propose that this observation can be explained by an intrinsic negative twist at the basal end which is untwisted and finally even reversed by the motion of the axoneme's dynein motors. It would be highly interesting to see whether this connection between torsion dynamics and structural twist can be corroborated, for example, by electron microscopy.

In contrast to existing multi-plane fluorescence techniques which often suffer from limited photon budget and photo-bleaching, our imaging system can be utilized for long-time 3D measurements of living specimens. Another potential application is high precision and fast 3D tracking of unlabeled particles, similar to what has be recently demonstrated with a multi-plane fluorescence microscope [40]. Finally, combining our system with white light quantitative phase imaging could allow for retrieving the 3D distribution of a sample's refractive index [12].

Disclosures. The authors declare no conflicts of interest.

Supplemental document. See Supplement 1 for supporting content.

References

1. J. Hernandez and S. Abrahamsson, "Multifocus structure illumination microscopy," Biophys. J. **116**(3), 282a–283a (2019).
2. S. Abrahamsson, J. Chen, B. Hajj, S. Stallinga, A. Y. Katsov, J. Wisniewski, G. Mizuguchi, P. Soule, F. Mueller, C. D. Darzacq, X. Darzacq, C. Wu, C. I. Bargmann, D. A. Agard, M. Dahan, and M. G. L. Gustafsson, "Fast multicolor 3D imaging using aberration-corrected multifocus microscopy," Nat. Methods **10**(1), 60–63 (2013).
3. S. Abrahamsson, M. McQuilken, S. B. Mehta, A. Verma, J. Larsch, R. Ilic, R. Heintzmann, C. I. Bargmann, A. S. Gladfelter, and R. Oldenbourg, "Multifocus polarization microscope (mf-polscope) for 3D polarization imaging of up to 25 focal planes simultaneously," Opt. Express **23**(6), 7734–7754 (2015).
4. S. Abrahamsson, R. Ilic, J. Wisniewski, B. Mehl, L. Yu, L. Chen, M. Davanco, L. Oudjedi, J.-B. Fiche, B. Hajj, X. Jin, J. Pulupa, C. Cho, M. Mir, M. E. Beheiry, X. Darzacq, M. Nollmann, M. Dahan, C. Wu, T. Lionnet, J. A. Liddle, and C. I. Bargmann, "Multifocus microscopy with precise color multi-phase diffractive optics applied in functional neuronal imaging," Biomed. Opt. Express **7**(3), 855–869 (2016).

5. S. Abrahamsson, H. Blom, A. Agostinho, D. C. Jans, A. Jost, M. Müller, L. Nilsson, K. Bernhem, T. J. Lambert, R. Heintzmann, and H. Brismar, "Multifocus structured illumination microscopy for fast volumetric super-resolution imaging," Biomed. Opt. Express **8**(9), 4135–4140 (2017).
6. M. S. Itano, M. Bleck, D. S. Johnson, and S. M. Simon, "Readily accessible multiplane microscopy: 3D tracking the HIV-1 genome in living cells," Traffic **17**(2), 179–186 (2016).
7. B. J. Walker and R. J. Wheeler, "High-speed multifocal plane fluorescence microscopy for three-dimensional visualisation of beating flagella," J. Cell Sci. **132**(16), jcs231795 (2019).
8. J. N. Hansen, A. Gong, D. Wachten, R. Pascal, A. Turpin, J. F. Jikeli, U. B. Kaupp, and L. Alvarez, "Multifocal imaging for precise, label-free tracking of fast biological processes in 3D," bioRxiv (2020).
9. K. F. Tehrani, C. V. Latchoumane, W. M. Southern, E. G. Pendleton, A. Maslesa, L. Karumbaiah, J. A. Call, and L. J. Mortensen, "Five-dimensional two-photon volumetric microscopy of in-vivo dynamic activities using liquid lens remote focusing," Biomed. Opt. Express **10**(7), 3591–3604 (2019).
10. S. Geissbuehler, A. Sharipov, A. Godinat, N. L. Bocchio, P. A. Sandoz, A. Huss, N. A. Jensen, S. Jakobs, J. Enderlein, F. G. van der Goot, E. A. Dubikovskaya, T. Lasser, and M. Leutenegger, "Live-cell multiplane three-dimensional super-resolution optical fluctuation imaging," Nat. Commun. **5**(1), 5830 (2014).
11. J. F. Jikeli, R. Pascal, L. Alvarez, and R. Honnef, "Patent 102010049751," (2010).
12. A. Descloux, K. S. Grußmayer, E. Bostan, T. Lukes, A. Bouwens, A. Sharipov, S. Geissbuehler, A.-L. Mahul-Mellier, H. A. Lashuel, M. Leutenegger, and T. Lasser, "Combined multi-plane phase retrieval and super-resolution optical fluctuation imaging for 4D cell microscopy," Nat. Photonics **12**(3), 165–172 (2018).
13. K. H. Bui, T. Yagi, R. Yamamoto, R. Kamiya, and T. Ishikawa, "Polarity and asymmetry in the arrangement of dynein and related structures in the *Chlamydomonas* axoneme," J. Cell Biol. **198**(5), 913–925 (2012).
14. C. J. Brokaw and R. Kamiya, "Bending patterns of *Chlamydomonas* flagella: IV. Mutants with defects in inner and outer dynein arms indicate differences in dynein arm function," Cell Motil. Cytoskeleton **8**(1), 68–75 (1987).
15. J. Lin and D. Nicastro, "Asymmetric distribution and spatial switching of dynein activity generates ciliary motility," Science **360**(6387), eaar1968 (2018).
16. C. J. Brokaw, "Direct measurements of sliding between outer doublet microtubules in swimming sperm flagella," Science **243**(4898), 1593–1596 (1989).
17. T. Sanchez, D. Welch, D. Nicastro, and Z. Dogic, "Cilia-like beating of active microtubule bundles," Science **333**(6041), 456–459 (2011).
18. V. Geyer, "Characterization of the flagellar beat of the single cell green alga *Chlamydomonas reinhardtii*," Ph.D. thesis, Sächsische Landesbibliothek-Staats-und Universitätsbibliothek Dresden (2013).
19. A. Edelstein, N. Amodaj, K. Hoover, R. Vale, and N. Stuurman, "Computer control of microscopes using μManager," Curr. Protoc. Mol. Biol. **92**(1), 14.20.1–14.20.17 (2010).
20. E. Wolf, "Electromagnetic diffraction in optical systems I. An integral representation of the image field," Proc. R. Soc. Lond. A **253**(1274), 349–357 (1959).
21. B. Richards and E. Wolf, "Electromagnetic diffraction in optical systems II. Structure of the image field in an aplanatic system," Proc. R. Soc. Lond. A **253**(1274), 358–379 (1959).
22. Q. Kemao, "Windowed Fourier transform for fringe pattern analysis," Appl. Opt. **43**(13), 2695–2702 (2004).
23. S. Montrésor, P. Memmolo, V. Bianco, P. Ferraro, and P. Picart, "Comparative study of multi-look processing for phase map de-noising in digital fresnel holographic interferometry," J. Opt. Soc. Am. A **36**(2), A59–A66 (2019).
24. Q. Kemao, "Windowed Fourier transform for fringe pattern analysis (with GUI)," https://www.mathworks.com/matlabcentral/fileexchange/24892-windowed-fourier-transform-for-fringe-pattern-analysis-with-gui.
25. S. C. Stein, A. Huss, D. Hähnel, I. Gregor, and J. Enderlein, "Fourier interpolation stochastic optical fluctuation imaging," Opt. Express **23**(12), 16154–16163 (2015).
26. G. B. Witman, "Isolation of *Chlamydomonas* flagella and flagellar axonemes," in *Meth. Enzymology*, vol. 134 (Elsevier, 1986), pp. 280–290.
27. J. Alper, V. Geyer, V. Mukundan, and J. Howard, "Reconstitution of flagellar sliding," in *Meth. Enzymology*, vol. 524 (Elsevier, 2013), pp. 343–369.
28. C. Xu and J. L. Prince, "Gradient vector flow: A new external force for snakes," in *IEEE Proc. CVPR*, (IEEE, 1997), pp. 66–71.
29. C. Xu and J. L. Prince, "Snakes, shapes, and gradient vector flow," IEEE Trans. on Image Process. **7**(3), 359–369 (1998).
30. S. Isbaner, A. Gholami, J. Enderlein, and I. Gregor, "Matlab code and example data for axoneme tracking in multi-plane microscopy," Torsional Dynamics in Flagellar Motion (2021), https://projects.gwdg.de/documents/1281.
31. M. P. Do Carmo, *Differential Geometry of Curves and Surfaces: Revised and Updated Second Edition* (Courier Dover Publications, 2016).
32. J. Lighthill, "Flagellar hydrodynamics," SIAM Rev. **18**(2), 161–230 (1976).
33. J. Elgeti, U. B. Kaupp, and G. Gompper, "Hydrodynamics of sperm cells near surfaces," Biophys. J. **99**(4), 1018–1026 (2010).
34. J. S. Hyams and G. G. Borisy, "Isolated flagellar apparatus of *Chlamydomonas*: characterization of forward swimming and alteration of waveform and reversal of motion by calcium ions in vitro," J. Cell Sci. **33**, 235–253 (1978).

35. C. J. Brokaw, "Computer simulation of flagellar movement VIII: coordination of dynein by local curvature control can generate helical bending waves," Cell Motil. Cytoskeleton **53**(2), 103–124 (2002).

36. P. Sartori, V. F. Geyer, J. Howard, and F. Jülicher, "Curvature regulation of the ciliary beat through axonemal twist," Phys. Rev. E **94**(4), 042426 (2016).

37. J. Lin, K. Okada, M. Raytchev, M. C. Smith, and D. Nicastro, "Structural mechanism of the dynein power stroke," Nat. Cell Biol. **16**(5), 479–485 (2014).

38. S. K. Dutcher, "Asymmetries in the cilia of *Chlamydomonas*," Philos. Trans. R. Soc., B **375**(1792), 20190153 (2020).

39. D. M. Woolley and G. G. Vernon, "Alternating torsions in a living "9+2" flagellum," Philos. Trans. R. Soc., B **266**(1425), 1271–1275 (1999).

40. B. Louis, R. Camacho, R. Bresolí-Obach, S. Abakumov, J. Vandaele, T. Kudo, H. Masuhara, I. G. Scheblykin, J. Hofkens, and S. Rocha, "Fast-tracking of single emitters in large volumes with nanometer precision," Opt. Express **28**(19), 28656–28671 (2020).